Modelling of Integrated Magnetic Components for Power Electronics

H.Njiende, N. Fröhleke† and W.A. Cronje‡
†Institute for Power Electronics and Electrical Drives, University of Paderborn, FB-14 LEA,
Pohlweg 47-49, 33098 Paderborn, Germany,
Phone & Fax: +49 5251 60 38 81, e-mail: njiende@lea.upb.de, froehleke@lea.upb.de,
‡Rand Afrikaanse University, P.O. Box 524, Aucland Park, 2006, South Africa,
Phone & Fax: +27-11-489-2602, e-mail: wacronje@ieee.org

Abstract— **A modelling approach for complete integrated magnetic components for VRMs is presented, which is verified on a four winding component. The influence of the center leg and outer leg air gaps on inductances, coupling factors and output current ripple are discussed. Analytical and FEM modelling results based on the geometrical, material and winding data are compared to experimental results. The complete modeling of the integrated magnetic component, also required for input and output filter design, enables simplified integration into simulation tools thereby enabling pre-optimization before breadboarding.**

I. Introduction

The strong demand for more compact power supplies is well known and the situation is aggravated by decreasing operating voltages for processors (< 3.3 V) resulting in a rising demand for high conversion ratio DC/DC converters. This is evident in the telecommunication industry and elsewhere. The use of voltage regulator modules (VRM's) has now become an accepted standard and constant attempts are made to improve the construction, efficiency and other characteristics of such modules. The recently proposed use of integrated magnetic components promises significant advantages in this regard.[1], [2], [3], [4], [5]

Using integrated magnetic components in push pull forward converters with current-doubler rectifier, is an optimal solution for improving the topology efficiency and at the same time reducing volume and costs. Fig. 1 shows this converter topology proposed in [1][2]. Three magnetic components are used in this topology variant: A 3-winding transformer and two filter inductors. Size and costs of these discrete components (as given in Fig. 2) and high voltage stress on power semiconductor components yield a negative impact, when compared to other double ended topologies. Additionally, the interconnections between transformer secondary and the inductors, particularly at low voltage and high current, which represent one target application for these circuits, cause extra losses.

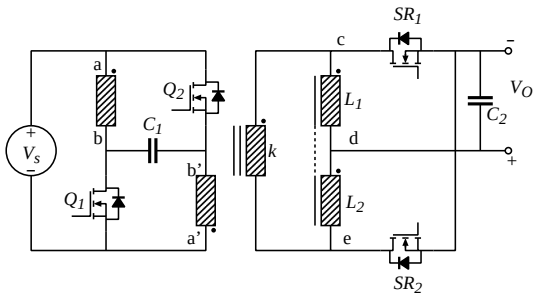

Fig. 1. Typical high conversion ratio topology;ie. push-pull forward.

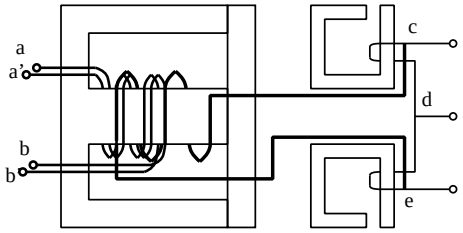

Fig. 2. Typical discrete magnetic components required for the topology under investigation .

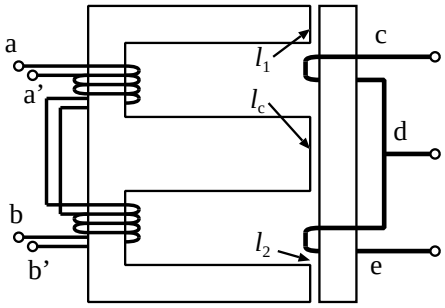

Fig. 3. Proposed integration of functionality, leading to a single four-winding device.

The primary windings are wound bifilarly, guaranteeing the tight coupling, essential for the push pull converter in order to reduce voltage stress on the primary sided MOSFETs. This is characterized by a very strong coupling of the split primary windings, each half of it in turn strongly coupled with the respective secondary winding.

Unfortunately the above mentioned publications have the following shortcomings: The complete inductance or coupling coefficient matrix of the integrated magnetics is not outlined and discussed; the center air gap dependence of secondary windings coupling coefficient and output current ripple is misinterpreted; the effect of microscopic inherent outer air gaps is not considered at all.

The modelling approach used here, for the integrated magnetic components, amounts to using the limb and air-gap reluctances to obtain analytical equations for the component. With the air-gaps as parameters the required coupling coefficients and other system information can be calculated. This approach is applied to a four winding component.

Analytical and FEM modeling results based on geometrical, material and winding data are compared to experimental results. The complete modelling of the integrated magnetic com-

$$L = \begin{bmatrix} \frac{n_{p1}^2 \cdot (R_1+R_2+4R_c)}{4\cdot\Delta} & \frac{n_{p1}\cdot n_{p2}\cdot (R_1+R_2+4R_c)}{4\cdot\Delta} & \frac{n_{p1}\cdot n_{s1}\cdot (R_2+2R_c)}{2\cdot\Delta} & \frac{n_{p1}\cdot n_{s2}\cdot (R_1+2R_c)}{2\cdot\Delta} \\ \frac{n_{p1}\cdot n_{p2}\cdot (R_1+R_2+4R_c)}{4\cdot\Delta} & \frac{n_{p2}^2\cdot (R_1+R_2+4R_c)}{4\cdot\Delta} & \frac{n_{s1}\cdot n_{p2}\cdot (R_2+2R_c)}{2\cdot\Delta} & \frac{n_{s2}\cdot n_{p2}\cdot (R_1+2R_c)}{2\cdot\Delta} \\ \frac{n_{p1}\cdot n_{s1}\cdot (R_2+2R_c)}{2\cdot\Delta} & \frac{n_{p2}\cdot n_{s1}\cdot (R_2+2R_c)}{2\cdot\Delta} & \frac{n_{s1}^2\cdot (R_2+R_c)}{\Delta} & \frac{n_{s1}\cdot n_{s2}\cdot R_c}{\Delta} \\ \frac{n_{p1}\cdot n_{s2}\cdot (R_1+2R_c)}{2\cdot\Delta} & \frac{n_{p2}\cdot n_{s2}\cdot (R_1+2R_c)}{2\cdot\Delta} & \frac{n_{s1}\cdot n_{s2}\cdot R_c}{\Delta} & \frac{n_{s2}^2\cdot (R_1+R_c)}{\Delta} \end{bmatrix} \quad (1)$$

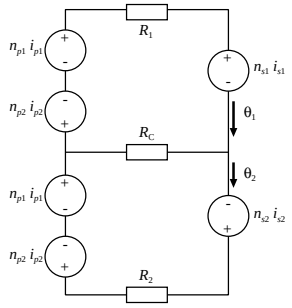

Fig. 4. Simplified reluctance model for the integrated four-winidng component. The three reluctances R_1, R_2 and R_c are mainly controlled by the corresponding air-gaps ie the gap lengths l_1, l_2 and l_c.

ponent, also required for input and output filter design, leads to a simplified integration into simulation tools.

II. Modelling of integrated magnetics

An analytical model for the four-winding integrated component is based on the reluctances of the various flux paths. For this component the two fluxes θ_1 and θ_2 are indicated in Fig. 3 The reluctance R is in general defined as

$$R = \frac{l}{\mu A} \quad (2)$$

where l is the length of the magnetic path, μ is the permeability of the material and A is the cross-sectional area through which the flux propagates. These variables are in principle all distributed quantities and it takes some expereince to make appropriate estimations for the lumped model. Applying this analysis to the to the magnetic circuit as depicted in Fig. 4 yields the L-matrix in Equation (1), describing the integrated component in terms of limb and air-gap reluctances.

In equation (1) $\Delta = R_1 \cdot R_2 + R_1 \cdot R_c + R_2 \cdot R_c$. R_1, R_2 and R_c are the reluctances of outer legs and the center leg respectively. n_{p1}, n_{p2}, n_{s1} and n_{s2} are primary and secondary winding turns. The rows and columns of the matrix are in the order (p_1, p_2, s_1, s_2).

For a symmetrical structure (symmetric core: $R1 = R2 = R_0$ and symmetric primary and secondary windings: $n_{p1} = n_{p2} = n_p$ and $n_{s1} = n_{s2} = n_s$) the inductance matrix is simplified as shown below (3).

$$L = \begin{bmatrix} \frac{n_p^2}{2\cdot R_0} & \frac{n_p^2}{2\cdot R_0} & \vdots & \frac{n_p\cdot n_s}{2\cdot R_0} & \frac{n_p\cdot n_s}{2\cdot R_0} \\ \frac{n_p^2}{2\cdot R_0} & \frac{n_p^2}{2\cdot R_0} & \vdots & \frac{n_p\cdot n_s}{2\cdot R_0} & \frac{n_p\cdot n_s}{2\cdot R_0} \\ \cdots & \cdots & \cdots & \cdots & \cdots \\ \frac{n_p\cdot n_s}{2\cdot R_0} & \frac{n_p\cdot n_s}{2\cdot R_0} & \vdots & \frac{n_s^2\cdot (R_0+R_c)}{R_0(R_0+2\cdot R_c)} & \frac{n_s^2\cdot R_c}{R_0(R_0+2\cdot R_c)} \\ \frac{n_p\cdot n_s}{2\cdot R_0} & \frac{n_p\cdot n_s}{2\cdot R_0} & \vdots & \frac{n_s^2\cdot (R_0+R_c)}{R_0(R_0+2\cdot R_c)} & \frac{n_s^2\cdot R_c}{R_0(R_0+2\cdot R_c)} \end{bmatrix} \quad (3)$$

which can be further simplified under certain conditions to

$$L_s \approx \begin{bmatrix} \frac{n_p^2}{2\cdot R_0} & \frac{n_p^2}{2\cdot R_0} & \frac{n_p\cdot n_s}{2\cdot R_0} & \frac{n_p\cdot n_s}{2\cdot R_0} \\ \frac{n_p^2}{2\cdot R_0} & \frac{n_p^2}{2\cdot R_0} & \frac{n_p\cdot n_s}{2\cdot R_0} & \frac{n_p\cdot n_s}{2\cdot R_0} \\ \frac{n_p\cdot n_s}{2\cdot R_0} & \frac{n_p\cdot n_s}{2\cdot R_0} & \frac{n_s^2}{2R_0} & \frac{n_s^2}{2R_0} \\ \frac{n_p\cdot n_s}{2\cdot R_0} & \frac{n_p\cdot n_s}{2\cdot R_0} & \frac{n_s^2}{2R_0} & \frac{n_s^2}{2R_0} \end{bmatrix} \quad (4)$$

The coupling coefficients between primary and secondary windings (K_{ps}), between both secondary windings (K_{ss}) and leakage inductance between both secondary windings (Ll_{s1s2}) are now:

$$K_{ps} = \left(\frac{R_c + 2\cdot R_0}{2(R_0+R_c)}\right)^{\frac{1}{2}}, \quad (5)$$

$$K_{ss} = \frac{R_c}{R_0 + R_c} \quad (6)$$

and

$$Ll_{s1s2} = L_{s2s2} - L_{s1s2} = \frac{n_s^2}{R_0 + 2\cdot R_c} \quad (7)$$

Alternatively the various inductance and coupling coefficients can be obtained from FEM calculations. By using a 2D FEM analysis, the leakage fluxes in the 2D section are taken care of, because the actual field distributions are determined. The analysis procedure essentially entails calculating the stored magnetic field energy with each coil energized in succession to obtain the self-inductance for that coil.

The coupling inductances are then determined by energizing two coils at a time, first with the two fields in additive and then in subtractive orientation, by varying the polarity of excitation for one of the coils. The stored magnetic field energy in each case are used to determine two inductance values from which the coupling inductances are determined. This basically recreates the well known method for measuring coupling inductances in the laboratory.

One set of results from such a calculation procedure is depicted in Fig. 5. This shows the self-inductances for a primary L_{11} and a secondary winding L_{44} as well as the mutual inductance between the same windings L_{14} as a function of the two air-gap lengths l_o and l_c.

III. Analysis of the integrated component

The structure of the matrix L exhibits that all but the secondary inductances (self and mutual of both) are independent of the center leg and of course of air gap on the center leg. The coupling factor of both primary windings is one, since they are wound bifilar. In the underlying integrated component the main gap is allocated to the center leg. This leads to a much larger reluctance in the center leg than those in the outer legs, which are only due to the polishing process of the surface of the core halves.

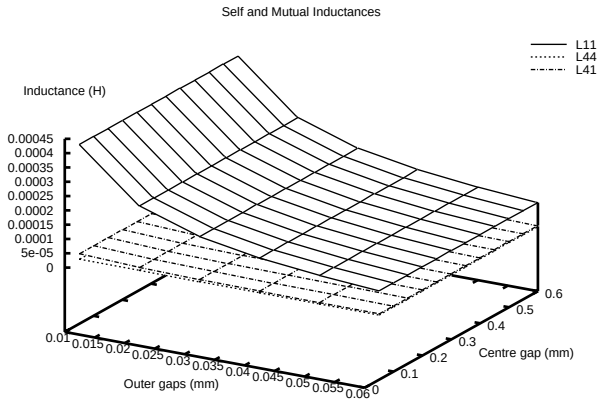

Fig. 5. Self-inductance L_{11}, self-inductance L_{44} and mutual inductance L_{41} obtained from FEM calculations.

The inductance matrix can be simplified further as shown in (4). L_s shows that the coupling coefficient of both secondary windings is close to one. This fully coupled structure (primary and secondary coupling coefficient equal to one) can also be obtained by splitting the secondary windings and wind each half on one outer leg. Indeed the split secondary solution is not plausible due to utilization of more than one turn, which will entail enlarged losses. Since there is some leakage flux between both secondary windings, the realistic coupling coefficient is less than 1.

Fig. 3 shows the final integrated magnetic component, with the leakage inductance between both secondary windings. Note that the self inductances of these windings are now utilized as the filter inductances.

Using the geometry of the core, the various reluctances can be computed and then the inductance and coupling coefficient matrices can be obtained.

Combining Equations (6) and (7) yields equation (8) and the output current ripple is therefore only related to the leakage inductance of the two coupled secondary inductors (as stated in [4]):

$$Ll_{s1s2} = \frac{n_s^2}{R_0} \cdot \frac{1-K_{ss}}{1+K_{ss}} \tag{8}$$

and

$$\Delta i_0 = \frac{2 \cdot V_0}{Ll_{s1s2} \cdot f_{sw}} \cdot (1-D) \tag{9}$$

where V_0 is the output voltage, f_{sw} the switching frequency and D the operation duty cycle.

For a coupling coefficient close to one the leakage inductance L_{ls1s2} will tend to zero and the output current ripple will rise to infinity. The leakage inductance is related to the coupling coefficient in (8) which in turn depends on the center leg air gap l_g. Accordingly, the output current ripple is related to the coupling coefficient as well as to the leakage inductance.

IV. Design Considerations and Experimental Results

The integrated magnetic components were built for a 48V - input, 1.6V/15A output push-pull forward converter with current doubler rectifier operated at a switching frequency of 200 kHz. Two geometrically diferent versions were investigated, a solenoidal (Fig. 6) and a planar (Fig. 7) version of the same functional four-winidng component. The differences in the respective inductance values is due to the use of standard core geometries and manufacturing problems that will be sorted out in due course.

A magnetic core EE25/13/8 carrying a solenoidal winding was chosen initially. An optimization according to [6] yields a planar ELP22/ELP22 of EPCOS AG. Each of these configurations have single turn secondary windings and twenty turn primary windings. The solenoidal component uses a litz of 105*0.1mm as primary winding material with ten turns on each outer leg and foil of 13mm*0.25mm as secondary windings, Fig. 6. For the planar component two paralleled layers of 70 mm each having five turns are used as primary windings and six paralleled one turn layers as secondary windings, Fig. 7. Depicted analytical results of both configurations match quite well the FEM results as well as the measurement results of built prototypes.

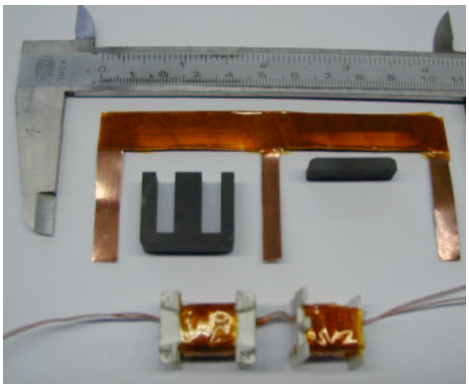

Fig. 6. Pre-assembly view of solenoidal construcion for the four-winding component.

The analytically calculated inductance matrix for the solenoidal component is

$$L_{analyt.} = \begin{bmatrix} 58.7 & 58.7 & 2.94 & 2.94 \\ 58.7 & 58.7 & 2.94 & 2.94 \\ 2.94 & 2.94 & 0.18 & 0.116 \\ 2.94 & 2.94 & 0.116 & 0.18 \end{bmatrix} \mu\text{H}.$$

The FEM calculated inductance matrix for the solenoidal component is

$$L_{FEM} = \begin{bmatrix} 68.35 & 68.32 & 3.42 & 3.42 \\ 68.32 & 68.35 & 3.42 & 3.42 \\ 3.42 & 3.42 & 0.19 & 0.15 \\ 3.42 & 3.42 & 0.15 & 0.19 \end{bmatrix} \mu\text{H}.$$

The measured inductance matrix for the solenoidal component is

$$L_{meas} = \begin{bmatrix} 53 & 52 & 1.98 & 2.135 \\ 52 & 53 & 2 & 1.93 \\ 1.98 & 2 & 0.13 & 0.065 \\ 2.13 & 1.93 & 0.065 & 0.15 \end{bmatrix} \mu\text{H}.$$

Good correspondence between the different calculated values and the measured values is observed for the solenoidal geometry.

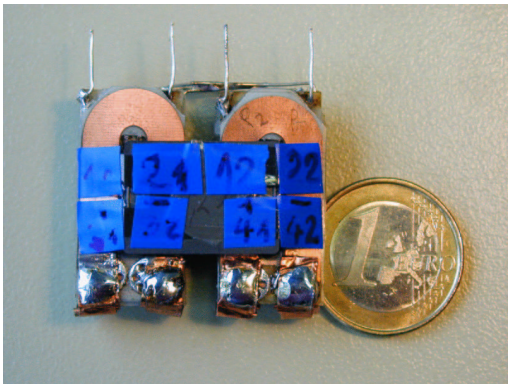

Fig. 7. Assembled view of the planar construcion for the four-winding component.

The Analytically calculated inductance matrix for the planar component is

$$L_{analyt.} = \begin{bmatrix} 435 & 435 & 21.75 & 21.75 \\ 435 & 435 & 21.75 & 21.75 \\ 21.75 & 21.75 & 1.28 & 0.89 \\ 21.75 & 21.75 & 0.89 & 1.28 \end{bmatrix} \mu\text{H}.$$

The FEM calculated inductance matrix for the planar component is

$$L_{FEM} = \begin{bmatrix} 402 & 402.5 & 20.25 & 20.25 \\ 402.5 & 402 & 20.25 & 20.25 \\ 20.25 & 20.25 & 1.12 & 0.887 \\ 20.25 & 20.25 & 0.887 & 1.12 \end{bmatrix} \mu\text{H}.$$

Measured inductance matrix for the planar component is

$$L_{meas} = \begin{bmatrix} 431 & 533 & 24.82 & 24.22 \\ 533 & 431 & 25.15 & 21.82 \\ 24.82 & 25.15 & 1.3 & 0.98 \\ 24.22 & 21.82 & 0.98 & 1.28 \end{bmatrix} \mu\text{H}.$$

Again good correspondence between the different calculated values and the measured values is observed, in this case for the planar geometry.

V. Simulations

The reluctance models derived above are readily integrated with the main circuit simulation in a program like SIMPLORER or the coupling coefficients can be used in SPICE and similar simulators. This makes it very simple to investigate the influence of the various air-gaps on the circuit performance.

Results are shown below for a simulation performed for the planar four-winding construction. In Fig. 8 the output current and voltage waveforms are shown. This would typically indicate to the designer whether the design specification is achieved. When supplying low-voltage microprocessors the allowable voltage ripple and transient response are strictly defined to ensure reliable operation.

In Fig. 9 the flux waveforms in the respective limbs is depicted. This information provides valuable insight into the behaviour of the magnetic component that cannot be achieved through measurements.

Because of lack of space design equations and guidelines will only be provided in the final paper. The inductance matrices are given as follows:

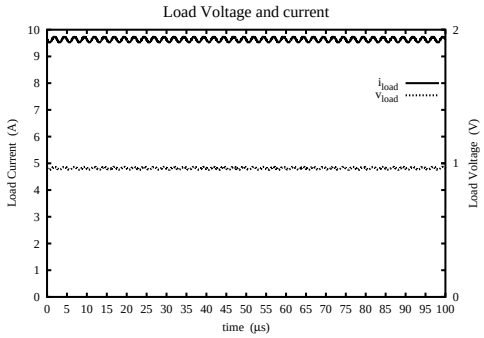

Fig. 8. Load (output) waveform. Here I_{load} close to 10 A and V_{load} close to 1 V as for a typical low voltage output application.

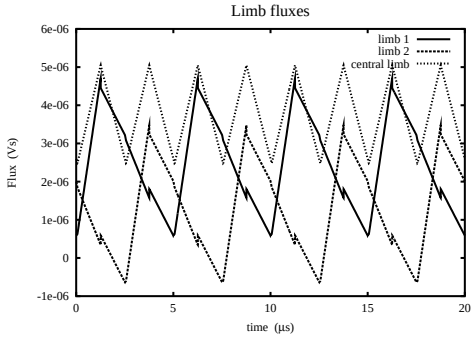

Fig. 9. Simulated flux waveforms for the central limb as well as the two outer limbs.

VI. Conclusions

It is concluded that the reluctance based analytical models are feasible for use in the modelling of integrated magnetic components. When compared to FEM calculations and measured values they provide acceptable results. The reluctance models lend themselve to incorporation in circuit simulators thereby enabling simulation of the complete circuit behaviour to determine the sensitivity to variation of paramaters such as the air-gaps.

Acknowledgment

Thanks belong to ASCOM Energy Systems for partly funding this investigation within project ”Low Voltage Power Supplies”.

References

[1] W. Chen, G. Hua, D. Sable, F. C. Lee, ”Design of High efficiency, low profile, low voltage converter with integrated magnetics,” IEEE APEC, 1997, pp. 911-917.

[2] P. Wong, Q. Wu, P. Xu, B. Yang and F.C. Lee, ”Investigating Coupling Inductor in Interleaving QSW VRM,” IEEE APEC, 2000, pp. 973-978.

[3] P. Xu, Q. Wu, P. Wong, and F. C. Lee, ”A Novel Integrated Current- Doubler Rectifier,” IEEE APEC, 2000.

[4] P. Xu and F.C. Lee, ”Design of High-Input Voltage Regulator Modules With A Novel Integrated Magnetics,” IEEE APEC, 2001.

[5] P. Xu, M. Ye and F. C. Lee, ”Single Magnetic Push-Pull Forward Converter Featuring Built-in Input Filter and Coupled-Inductor Current Doubler for 48V VRM,” IEEE APEC, 2002.

[6] N. Froehleke, H. Mundinger, H. Njiende, P. Wallmeier, H. Puder, ”CAE-Tool for Optimizing Development of Switched Mode Power Supplies,” IEEE APEC, 2001.

[7] H. Njiende, H. Wetzel, N. Froehleke and W. Cronje, ”Simulation of Power Converters Comprising Integrated Magnetic Components with SIMPLORER,” Proposed for IEEE APEC 2002.